Toward a Deep-Learning-Network-Based Convective Weather Initiation Algorithm From the Joint Observations of Fengyun-4A Geostationary Satellite and Radar for 0–1h Nowcasting

Fenglin Sun [ID], Bo Li [ID], Min Min [ID], and Danyu Qin

Abstract—Nowcasting of convective weather is a challenging and significant task in operational weather forecasting system. In this article, a new convolution recurrent neural network based regression network for convective weather prediction is proposed, which is named as the convective weather nowcasting net (CWNNet). The CWNNet adopts the joint observations of Fengyun-4A geostationary (GEO) satellite and the ground-based Doppler weather radar data of the last 0–1-h as the inputs of the model to predict the radar reflectivity factor maps of next 0–1 h. The statistical validating results clearly demonstrate that the mean values of the probability of detection, false alarm ratio, threat score, root mean square error and mean absolute error evaluating the performance of CWNNet for 1-h nowcasting reach 0.87, 0.137, 0.71, 3.365 dBZ and 1.038 dBZ, respectively. Due to that the GEO meteorological satellite is capable of capturing the features of convective initiation (CI), the CWNNet shows a good performance in CI nowcasting. Besides, several case studies also further indicate that the CWNNet can predict CI more than 30 min in advance by monitoring the convective clouds. The CWNNet based on the joint satellite and radar data shows a better nowcasting performance than that only employing single data source. Thus, it can effectively produce more reliable nowcasting for convective weather events.

Index Terms—Convective weather nowcasting, deep learning (DL), fengyun-4A geostationary (GEO) satellite, ground-based weather radar.

I. INTRODUCTION

NOWCASTING of severe convective weather events with strong destructive power has always attracted widespread attention [1], [2]. The timely and effective response to severe convective weather phenomena, such as heavy rain, thunder, heavy hail, and strong wind, is of vital importance to reduce substantial costs to human properties and lives [3], [4], [5], [6]. However, it is still very difficult to forecast the local and rapidly developing severe convective weather by using traditional numerical weather prediction (NWP) models due to the limits of spatiotemporal resolution.

In the recent decades, various advanced nowcasting techniques based on extrapolation algorithms using observation data from ground-based weather radar, the geostationary (GEO) meteorological satellite, or the NWP products have been widely developed and used to monitor or forecast severe convective systems, which once played very important roles in the operations of severe weather nowcasting [7], [8], [9], [10]. As one of the most effective tools and exclusive instruments for the nowcasting and diagnosis of convective weather events [11], [12], [13], the Doppler weather radar has been well developed and widely applied for monitoring and extrapolating severe weather [14], [15]. However, Doppler radar stations are distributed in limited areas and have no coverage for most oceanic and mountainous regions [16]. Monitoring the convection from the space-borne radar on GPM is indeed a good alternative. But, in contrast, its timeliness does not meet the requirements of real-time services.

It is well known that the GEO meteorological satellite imagery is one of the most effective means for monitoring convective weather, due to its unique ability to cover a wide region including oceanic and mountainous areas [17], [18], [19], [20], [21], [22]. Recently, the development of the new-generation GEO meteorological satellites, including GEO operational environmental Satellite-R, Himawari-8/9, Fengyun-4, significantly enhance their capabilities of nowcasting severe convective events by improving spatial-temporal resolutions and increasing more sensitive channels in wide spectral ranges [23], [24], [25]. Furthermore, the GEO meteorological satellites have the unique advantages of capturing the indications of convective initiation (CI), such as the cloud-top height, cloud-top glaciation, updraft strength and cloud-top cooling rate [26],

[27], [28]. At present, the relatively high false alarm ratio (FAR) is still the main problem in current nowcasting algorithms for CI by using continuous GEO meteorological satellite observations [29], [30], [31]. Nevertheless, a recent study explicitly illustrates that the combination of satellite and NWP products or radar data can further improve the CI nowcasting algorithms [10].

Object-oriented algorithms identify targets and correlate adjacent frames to find spatial differences. These differences are then used to predict motion and development [32], [33]. Similarly, the optical flow (OF) based method calculates the motion field between successive images based on the assumption of image brightness constancy. After that, the extrapolation is applied based on the trends of the motion field iteratively [34], [35]. Typical examples of tracking-based extrapolation systems include thunderstorm identification, tracking, analysis, and nowcasting (TITAN) [36], storm cell identification and tracking (SCIT) [37]. A novel cluster-based spatiotemporal regression method was also introduced to predict the satellite image sequence for weather nowcasting [38]. In addition, the forecast and tracking the evolution of cloud clusters method predicts the convective objects by considering the motion trend of the centroid of the cloud cluster and its size evolution from satellite imageries [39]. However, these well-used object-oriented tracking techniques are only able to predict the displacement of the convective cloud clusters for next 0–2 hours, while the evolution of their shapes and intensities are difficult to forecast. That is, these methods cannot identify the initiation, development and dissipation stages of storms, and thus fail in predicting the storm evolutions precisely.

In recent years, the advanced machine learning-based techniques provide new possibilities for the nowcasting of convective activities by using integrated applications with multisource data. The techniques of logistic regression, support vector machine and random forest have been developed to automatically identify the motion and growth/decay of thunderstorms. For example, some advanced machine learning-based techniques have been employed to perform the 0–2-h forecasts of severe convective events using data from radar, GEO satellite and NWP [40], [41], [42]. Besides, the deep learning (DL) methods have been already applied in the nowcasting of convective systems with significant progress. One of the representative forecasting approaches is the convolution recurrent neural network (ConvRNN) which combines the convolutional neural networks (CNN) with the recurrent neural network (RNN), such as the convolutional long short-term memory method for radar echo extrapolation and precipitation nowcasting [43], [44]. Several gate recurrent unit (GRU) based models (such as the generative adversarial-convolutional GRU and the trajectory GRU) are also proposed for precipitation nowcasting [45], [46]. Compared with the traditional machine learning-based algorithm, the DL networks can automatically extract the features of the convective systems from radar echoes and predict the evolution [47], [48], [49]. Furthermore, based on multisource data from radar, satellite, NWP, the DL networks demonstrate the ability in achieving effective and successful predictions on the CI, lightning and rapid evolving convective systems within the next hour [50],

[51], [52], implying that their performances are superior to those of traditional extrapolation methods.

In this investigation, an advanced DL-network-based algorithm is developed to predict the convective weather of the next 0–1-h by using joint observations of Fengyun-4A and ground-based radar. Although that the lifetime of convective weather nowcasting can be up to 2 h obtained through the convective weather nowcasting net (CWNNet), the statistical results clearly illustrate that the lead times of the most of CI are still concentrated in 30 min and the accuracy of CI nowcasting will be reduced greatly when the predictable period exceeds one hour [40], [52]. Therefore, this article mainly focuses on developing a 0–1-h convective weather nowcasting algorithm with regards to higher accuracy. Based on the joint observation data, the ConvRNN is introduced into this novel algorithm to capture the striking characteristics of rapidly spatial-temporal evolution or precursor of convective cloud system by taking advantage of its merit of profiling convective clouds at different stages.

The remainder of this article proceeds as follows. Section I introduces overview of the data from the GEO meteorological satellite and the ground-based weather radar. Section III presents the new DL-based methodology and framework for 0–1-h convective weather nowcasting. Section IV illustrates the validation results and several real cases. Finally, Section V summarizes the main conclusions.

II. DATA

A. Interest Fields From Fengyun-4A

As the first of China's second-generation GEO meteorological satellites, Fengyun-4A was successfully launched on December 11, 2016 and began operations since about the April of 2017. The advanced geosynchronous radiation imager (AGRI) including visible, near-infrared and infrared channels ranging from 0.47 to 13.5 μm (14 independent channels) is one of the main payloads of Fengyun-4A. With the nadir point located at 104.7°E, the observation of Fengyun-4A /AGRI covers the Asia, Oceania region, Indian Ocean. The spatial resolutions of this advanced spaceborne imaging system are 0.5–4 km for the visible channels and 4km for the infrared channels at nadir. Observation data from Fengyun-4A /AGRI can be regularly acquired with two different scanning operational maneuvers (15 min over the full-disk domain and 5-min over the continental China domain). Compared with China's first-generation GEO meteorological satellites (Fengyun-2), Fengyun-4A can significantly enhance the capabilities of early-warning and forecasting [18], as it benefits from increased spatial-temporal resolutions and high-precision radiation channels that are related to cloud-top physical properties such as the optical thickness, cloud temperature, hydrometeor phase, geometrical morphology and effective particle radius [53].

Table I gives the interest fields from Fengyun-4A /AGRI channels for the 0–1-h convective weather nowcasting models by the CWNNet. The specific reason for choosing these interest fields is that they are sensitive to the cloud-top microphysical composition [27], [54], [55]. The study of retrieving the radar

TABLE I
INTEREST FIELDS FROM FENGYUN-4A /AGRI FOR 0–1-HOUR CONVECTIVE
WEATHER NOWCASTING MODELS

No.	Interest Fields	Physical Basis	Model index
1	Modified albedo 0.65 μm	Optical depth	Model I
2	Albedo ratio 0.65/1.61 μm	Cloud-top glaciation/particle size	
3	Tb 10.8 μm	Cloud-top temperature assessment	
4	Tb 12.3–10.8 μm	Optical depth	Model II
5	Tb 10.8–8.5 μm	hydrometeor phase	
6	Tb 10.8 μm	Cloud-top temperature assessment	

*Note: the modified 0.65 μm albedo means albedo with Sun Zenith Angle (SZA) ≤60° and calibrated by the factor sec (SZA). Tb means brightness temperature.
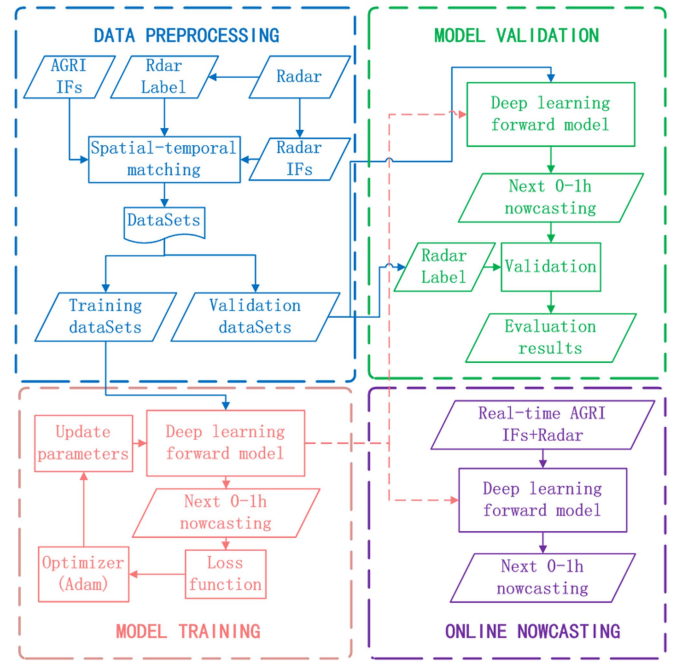

Fig. 1. Processing flowchart of the DL-based CWNNet algorithm by using the combination of Fengyun-4A /AGRI and radar data, including modules of data preprocessing (up-left), model validation (up-right), model training (down-left) and online nowcasting (down-right).

composite reflectivity factor (RCRF) from Fengyun-4A /AGRI interest fields has explored the spectral response of cloud top attributes and the sensitivity of these interest fields [56]. The statistical results show that visible models exhibit a better performance of retrieving RCRF. To comprehensively evaluate the potential for 0–1-h convective weather nowcasting system, this article also proposes these two independent models to investigate the differences between visible/near-infrared and infrared channels.

B. Ground-Based Weather Radar Data

The reflectivity factors derived from the Doppler weather radar echo data have been widely utilized to analyze the cloud and hydrometeor distribution of severe weather phenomena. The mosaic maps of RCRF provided by the China Meteorological Administration (CMA) are also used as the input for the 0–1-h nowcasting model. The RCRF maps at next 0–1-h as the ground truth for the model training and validating. The imagery products derived from radar composite reflectivity used in this investigation are obtained from the ground-based weather radar website of China (http://data.cma.cn). To exactly determine the detailed three-dimensional (3-D) structure of thunderstorm, the radar tilts to several elevation angles above the horizon and makes a 360° horizontal scanning for each fixed elevation angle. The RCRF is the maximum base reflectivity value representing the most intense portions of thunderstorms in a given vertical column within the radar scanning area. It has a horizontal resolution of 0.01° × 0.01° with an interval of 6 minutes.

III. METHODOLOGY

A. Processing Flow

The processing flow of this new algorithm for 0–1-h convective weather nowcasting developed in this investigation consists of four key parts, including data preprocessing, model training, model validation, and online nowcasting (see the flowchart in

Fig. 1). In the data preprocessing module, Fengyun-4A /AGRI and radar data will be spatially and temporally collocated and separated into training, validation, and test datasets. The training dataset is used for fitting the model's learnable parameters (e.g., weights of connections between neurons in artificial neural networks) of nowcasting model. The training module involves the selection and calculation of loss function with the optimizer. In each training iteration, the coefficients of the network model will be updated by the optimization algorithm. Note that, after the training, the trained model parameters will be shared with model validation and online nowcasting modules. The validation dataset provides an unbiased evaluation of a model fit on the training dataset with the optimized model's hyper parameters. The validation datasets can also be used for regularization by early stopping to avoid the overfitting. To accurately evaluate the performance of prediction model, the independent test dataset in validation module is used to provide an unbiased evaluation on a final model. The online nowcasting module will conduct the 0–1-h nowcasting in real time by using the well-trained prediction model mentioned before.

B. Training and Validation Data Collecting

The joint observations of Fengyun-4A /AGRI and ground-based radar are used as the input for the DL-based 0–1-h convective weather nowcasting algorithm, while the radar data of next 0–1-h as the ground truth. First, the quality control procedure is performed for both satellite and radar data. Incomplete satellite and radar data with lost lines will be eliminated directly. Second, pixel-level multisource data fusion involves geocoding and interpolation of the images to a common grid. In this investigation,
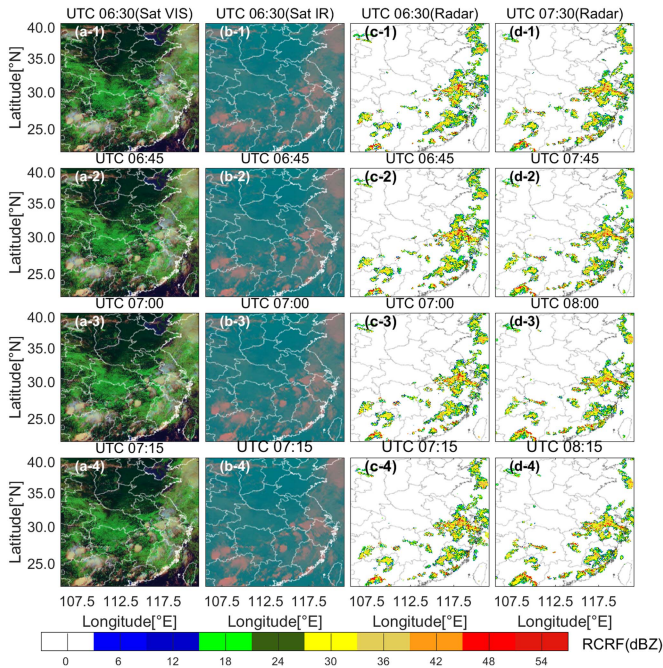
Fig. 2. Input and output for the 0–1-h nowcasting of CWNNet from 06:30 to 08:15 UTC on June 10, 2020. (a) Pseudo color maps constructed by normalized interest fields from model I as part of the input, (b) pseudocolor maps constructed by normalized interest fields from model II as part of the input, (c) the mosaic RCRF maps as another part of the input at the same time, and (d) the mosaic RCRF maps of the next 0–1-h as the ground truth.

the values of radar reflectivity factor are averaged in horizontal space to match the observation resolution of Fengyun-4A /AGRI pixel. For each radar image the closest matching nowcasting image in time is chosen. Since the ground-based weather radars conduct scanning mode within a 6-min interval, the maximum temporal mismatch between the datasets is thus 3 min, which is at a movement velocity of cloud of e.g., 20 m/s will result in a 3.6 km mismatch in the observed features. Finally, after the data fusion, the strong radar echo samples in clear sky determined by the matched Fengyun-4A /AGRI operational cloud mask products [53] will be deleted.

Fig. 2 shows a case involving the input and output of the CWNNet. The study domain in this investigation contains parts of China (22.5°N–40°N, 105°E–120°E) which is fully covered by radar echo. Fig. 2(a) and (b) displays the pseudo color maps constructed by normalized interest fields from models I and II as part of the inputs, respectively. Fig. 2(c) shows the RCRF maps at the same time. Fig. 2(d) shows the RCRF maps of the next 0–1-h as the ground truth. This square domain is divided into 400 × 400 grids with a spatial resolution of 4 km × 4 km. The input multi-dimensional matrix for the training model has a shape of $N_{\text{batch}} \times N_s \times N_{\text{ch\_in}} \times H \times W$ (12 × 4 × 4 × 400 × 400), where N_{batch} is the batch size of the training samples to balance the local optimization of samples and the speed of training; N_s is the length of sequencer; $N_{\text{ch\_in}}$ is the input channel number of joint observations of satellite and radar data for the CWNNet; H and W are, respectively, the height and width of satellite imagery covering the study area. Moreover, the output of the prediction model is also a multi-dimensional

Application	Model I		Model II	
Month	Training	Validation	Training	Validation
Mar.	783	168	1750	421
Apr.	1221	262	1437	356
May.	1302	279	1564	368
Jun.	1271	272	1736	399
Jul.	1397	299	1864	436
Aug.	1259	270	1716	428
Sept.	1176	252	1229	268
Oct.	949	203	1302	317

matrix with a shape of $N_{\text{batch}} \times N_s \times N_{\text{ch\_out}} \times H \times W$ (12 × 4 × 1 × 400 × 400), where $N_{\text{ch\_out}}$ is the channel number of the radar binary masks. It is worth mentioning that for convenience, scenario IR and scenario VIS are short for the interest fields from satellite infrared channels combined with radar and the interest fields from satellite visible channels combined with radar, respectively.

Table II gives the monthly sample numbers for model training and validation. Note that to prevent the data leakage, the training samples are isolated from the validation samples. The datasets are arranged in chronological order. The first two-thirds of datasets of each month are used as the training samples, the next one-sixth as the testing samples and the remained one-sixth as the validation samples.

C. Network Architecture

The mathematical model for the 0–1-h convective weather prediction problem can be described as follows:

$$\tilde{\tilde{j}}_{t+1}, \ldots, \tilde{\tilde{j}}_{t+K}$$
$$= \underset{J_{t+1}, \ldots, J_{t+K}}{\arg \max} \ p\left(J_{t+1}, \ldots, J_{t+K} | I_{t-n+1}, \ldots, I_t\right) \quad (1)$$

where $(I_{t-n+1}, I_{t-n+2}, \ldots, I_t)$ are the historical 0–1-h observation status of AGRI and radar from $t - n + 1$ to t; $(J_{t+1}, \ldots, J_{t+K})$ are the next 0–1-h predicted RCRF maps from $t + 1$ to $t + K$. As illustrated in Fig. 3, this article introduces the ConvRNN model to solve this problem. The backbone of CWNNet is evolved from the ConvRNN encoder and decoder models [44]. Both the encoder and decoder are constructed by three stacked layers of ConvRNN at different scales. The RNN model captures the temporal dynamics of the hidden states into the temporal memory, while the CNN is used to extract the spatial-spectral information.

In addition, the CWNNet adds a spatial memory module on the basis of ConvRNN. As illustrated in Fig. 4, the input of this ConvRNN block contains the current input X_t, spatial memory M_t^{l-1}, temporal memory C_t^{l-1} and hidden state H_t^{l-1} (at time t and layer $l - 1$). The calculation of the RNN unit is expressed as

$$i_t = \sigma\left(W_{xi} * X_t + W_{hi} * H_{t-1}^l + b_i\right)$$
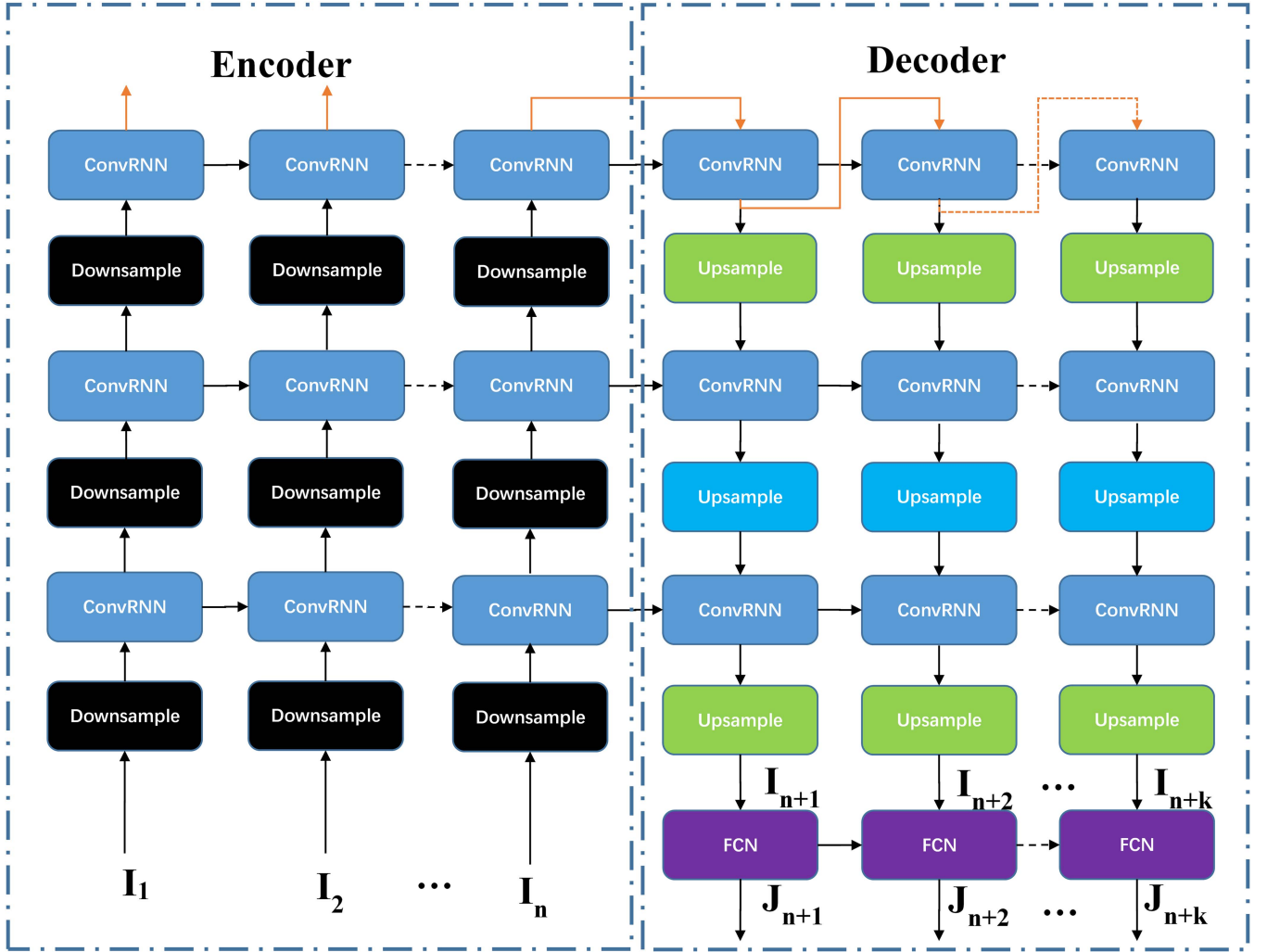$$g_t = \tan h\left(W_{xg} * X_t + W_{hg} * H_{t-1}^l + b_g\right)$$
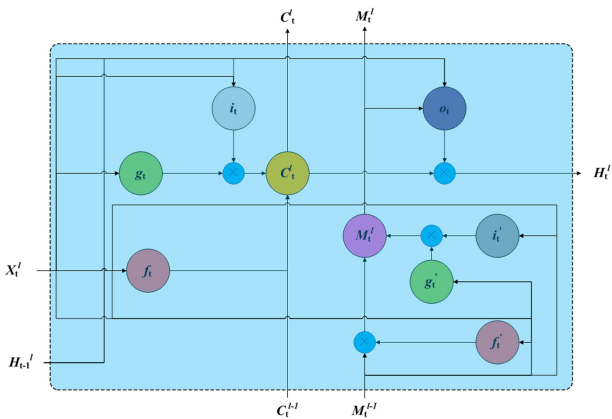
Fig. 3. Architecture of the CWNNet model.

Fig. 4. Inside structure of the ConvRNN unit for the CWNNet model.

$$f_t = \sigma \left(W_{xf} * X_t + W_{hf} * H_{t-1}^l + b_f \right)$$

$$i_t' = \sigma \left(W_{xi}' * X_t + W_{mi} * M_t^{l-1} + b_i' \right)$$

$$g_t' = \tan h \left(W_{xg}' * X_t + W_{mg} * M_t^{l-1} + b_g' \right)$$

$$f_t' = \sigma \left(W_{xf}' * X_t + W_{mf} * M_t^{l-1} + b_f' \right)$$

$$C_t^l = i_t \circ g_t + f_t \circ C_{t-1}^l,$$

$$M_t^l = i_t' \circ g_t' + f_t' \circ M_t^{l-1}$$

$$o_t = \sigma \left(W_{xo} * X_t + W_{ho} * H_{t-1}^l \right.$$
$$\left. \times + W_{co} * C_t^l + W_{mf} * M_t^l + b_o \right)$$

$$H_t^l = o_t \circ \tan h \left(W_{1 \times 1} * \left[X_t^l, M_t^l \right] \right) \qquad (2)$$

where $\circ$, $*$, and σ denote Hadamard product, 2-D convolution and sigmoid function, respectively; $tanh$ is the hyperbolic tangent function and the Layer Norm is layer normalization that stabilizes the training processing; i_t, g_t, f_t, and o_t are the input gate, cell, forget gate, and output gate, respectively.

In the encoder section, the process of downsampling is to reduce the size of the feature-maps by a factor of 2 with the method of maxpooling. The forecaster section is approximately a mirror image of the encoder section. The process of upsampling is to enhance the size of the feature-maps by a factor of 2 with the method of bilinear.
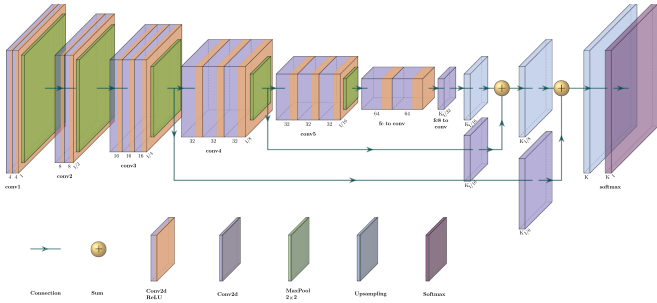
Fig. 5. Output transforming structure of the FCN for the CWNNet model.

The final output module of the CWNNet model is a lightweight fully convolutional network (FCN) which transforms the predicted feature maps into the predicted RCRF maps. In fact, the FCN bases on another state-of-the-art network called VGG-16 and plays an important role in target segmentation and regression [57]. As shown in Fig. 5, the FCN consists of the repeated application of six layers for the encoder. At each level of the encoder, two or three convolution operations are performed with a batch normalization and rectified linear unit (ReLU) activation function. Then, a max pooling downsample operation with a stride of 2 is appended. In the decoder part, every step consists of an upsampling of the feature map followed by summing a concatenation with the correspondingly cropped feature map from the encoder part. At the final layer, a 1×1 convolution layer with the ReLU activation function is used to map the last feature vectors to the desired RCRF value. The encoder-decoder network has 15 independent convolutional layers in total.

D. Model Training

All the models were built in Pytorch. Models were trained on a single machine with 12 CPU cores and 2 NVIDIA TITAN RTX GPUs. To optimize the model parameters, the adaptive moment estimation (Adam) of Pytorch (an optimized tensor library for DL) was employed to speed up training tasks [58]. The learning rate was set to 0.0001 with a high momentum of 0.999. Accordingly, L_1 regularization was also introduced to avoid the over fitting of the model. For training, the cost function is computed by a pixel-wise root-mean-square error (RMSE) combined with mean absolute error (MAE)

$$L = \sqrt{\frac{1}{N}\sum_{i=1}^{N}(y_i - y_{\text{pred},i})^2} + \sum_{i=1}^{N}|y_i - y_{\text{pred},i}|/N \quad (3)$$

where y_i and $y_{\text{pred},i}$ are the pixels of the true data and the predicted RCRF maps, respectively. To avoid overfitting in training model, we force to stop training when the error in the validation dataset increases, as this is a typical sign of overfitting to the training dataset.

Moreover, we also introduce the pixel-wise threat score (TS), probability of detection (POD) and FAR as reference indicators to evaluate the performance of the CWNNet model. The specific validation procedure for the results retrieved or predicted by

TABLE III
CONTINGENCY TABLE

		Observed value	
		RCRF>0	RCRF =0
Forecast	RCRF>0	True Positive (TP)	False Positive (FP)
value	RCRF=0	False Negative (FN)	True Negative (TN)

Once the contingency tables are populated, statics are computed (see Table IV).

TABLE IV
STATISTICAL METRICS FOR CWNNET

Name	Formula	Range	Optimum
POD	TP/(TP+FN)	[0,1]	1
FAR	FP / (TP+ FP)	[0,1]	0
TS	TP/(TP+FP+FN)	[0,1]	1

The meanings of TP, FN, FP, and TN are given in Table III.
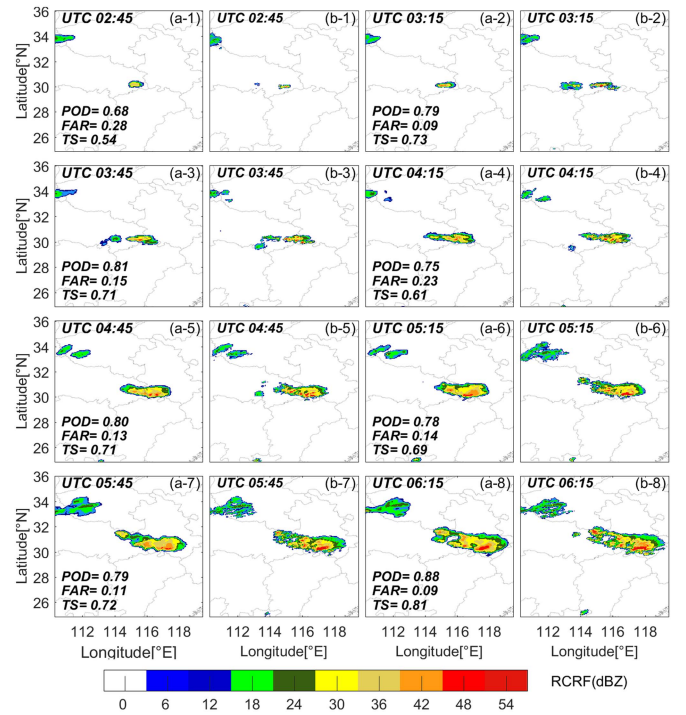

Fig. 6. (a) Predicted RCRF maps of 1-h convective weather nowcasting from the CWNNet (b) the corresponding observed RCRF data from ground-based weather doppler radars on March 21, 2020 (the skill scores are also given in each subfigure). Generally, "*b*-I" was one of the inputs used to generate "*a*-(*i*+2)."

the CWNNet is based on a dichotomous forecast verification technique. The equations for the three metrics are given in Tables III and IV.

IV. RESULTS AND DISCUSSIONS

A. Case Studies

Fig. 6 displays a series of developing severe convective weather events occurring in Hubei Province and Anhui Province (110°E–118°E, 29°N–35°N) of China, and the probabilistic results of the 1-h nowcasting by the CWNNet of scenario VIS for these convective weather events during different stages,
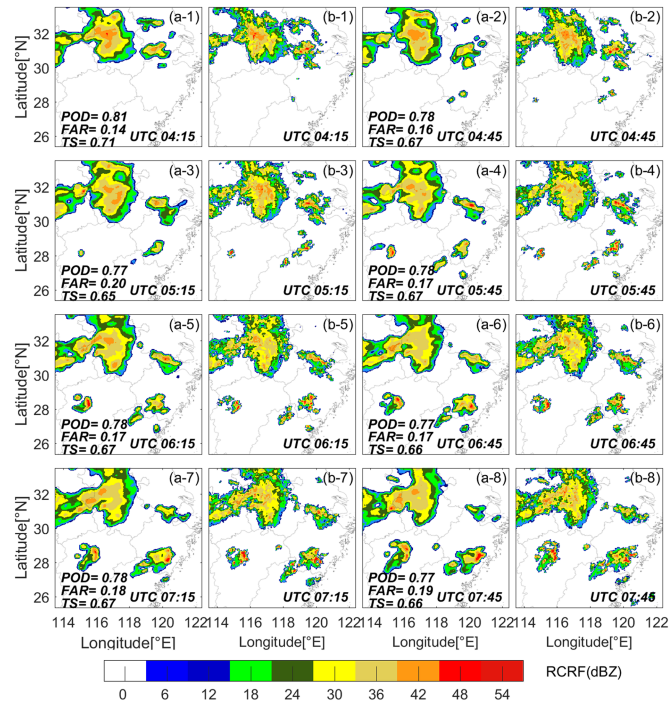
Fig. 7. (a) Predicted RCRF maps of 1-hour convective weather nowcasting from the CWNNet. (b) Corresponding observed RCRF data from ground-based weather Doppler radars on June 22, 2020 (the skill scores are also given in each subfigure).

Fig. 8. 0–1-hour nowcasting at 03:15 UTC on July 29, 2020 by the CWNNet. Contours indicate the probabilistic nowcasting of convections, and the shaded areas are the RCRF at (a) 03:30 UTC, (b) 03:45 UTC, (c) 04:00 UTC, and (d) 04:15 UTC, respectively.

Fig. 9. 0–1-h nowcasting at 03:45 UTC on July 29, 2020 by the CWNNet; contours present the probabilistic nowcasting of convections, and the shaded areas are the RCRF at (a) 04:00 UTC, (b) 04:15 UTC, (c) 04:30 UTC, and (d) 04:45 UTC, respectively.

including the initiation and mature stages. In the southeast of Hubei Province, two convective cells occurred at 02:45 UTC on March 21, 2020, which developed quickly and extended southeastward within 30 min. Moreover, one convective cell even reached the borders of Hubei Province and Anhui Province. From 03:45 UTC to 04:15 UTC, these two cells merged into one target gradually. This system reached the border of Jiangsu Province and Zhejiang Province at 06:15 UTC. The mean values of the POD, FAR, and TS for this case amount to 0.785, 0.153, and 0.691, respectively.

On June 22, 2020, some severe convective activities occurred in eastern China (114°E–122°E, 26°N–34°N), which started at about 04:30 UTC, then grew up quickly and extended to the southwest. At 05:00 UTC, a new convective cloud cell was formed in the west of Jiangxi Province centered at (115°E, 28°N), which developed synchronously with the previous one. At 08:00 UTC, both of the two systems developed into the mature stage. The probabilistic results of 0–1-h nowcasting by CWNNet and the corresponding observed RCRF data for this case are presented in Fig. 7. The results show that the CWNNet performed well in predicting the convective storm during different stages, including the stages of initiation and intensification. The average values of the POD, FAR and TS for this case are 0.781, 0.1725, and 0.672, respectively.

Besides, some typical cases focused on the CI stages are also selected to further evaluate the nowcasting performance of CWNNet. This case occurred in southeast China on July 29, 2020, where thermal convections frequently generates in climatology. As shown in Fig. 8, ten isolated convective cells labeled
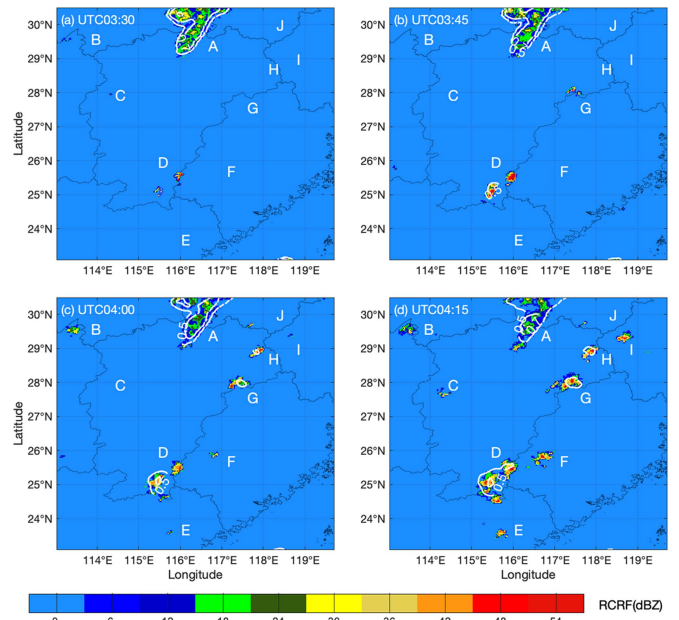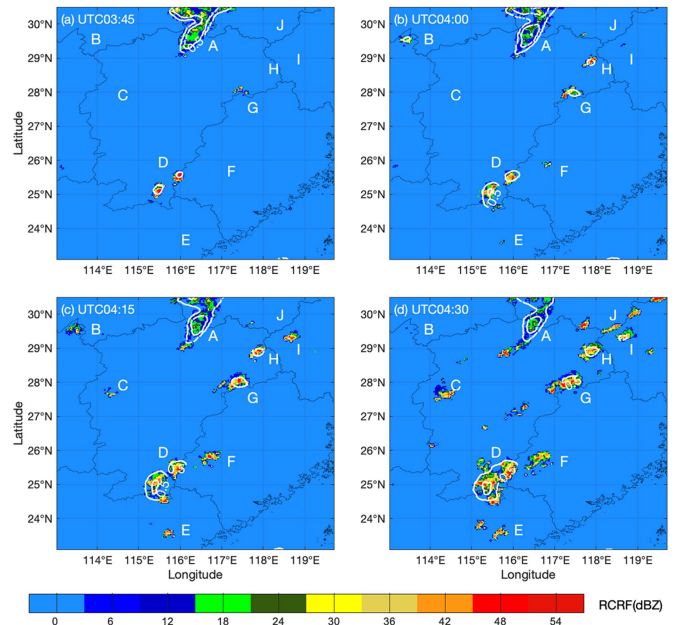
"A" to "J" initiated or developed from 03:30 UTC to 04:15 UTC. The radar-reflectivity maps at 03:30 UTC revealed that system "A" was already at its mature stage. Two isolated targets initiated in the inner position of marked target "D," but there was no indication that these two targets were going to merge into one target, and neither any other system would form. At 03:45 UTC
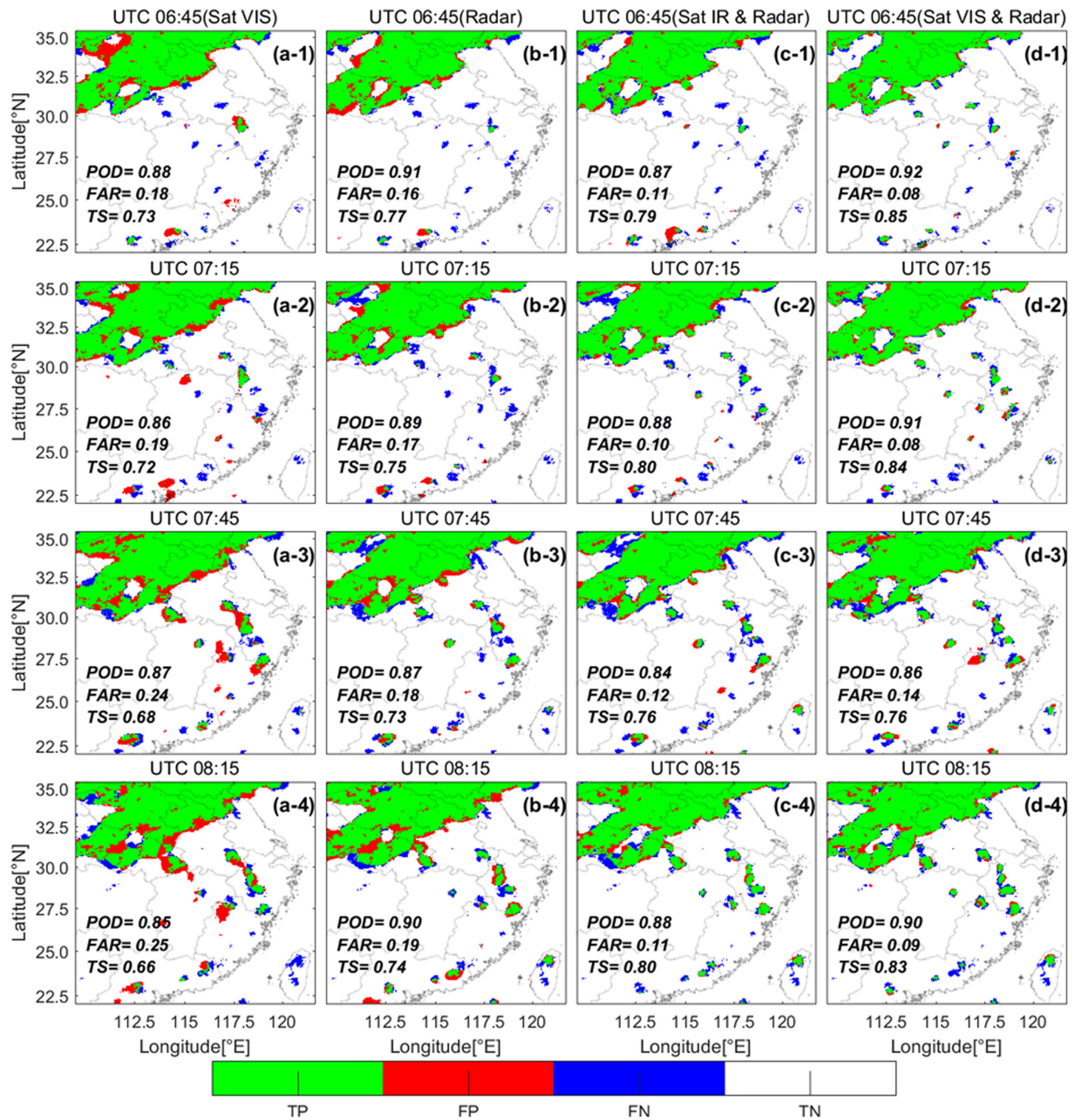
Fig. 10.   Contingency table results of comparative experiments of 1-h nowcasting from 06:45 UTC to 08:15 UTC on June 28, 2019 by using the interest fields from different sources. The subplots at each row of the panel are the elements of contingency table for statistical metrics of the CWNNet's 1-hour nowcasting, with interest fields of (a) satellite visible channels, (b) radar, (c) scenario IR, and (d) scenario VIS. The elements of contingency table including "TP" (green), "FP" (red), "FN" (blue) and "TN" (white) are defined in Table III. The green + blue is the pattern where the observed RCRF>0.

[see Fig. 8(b)], system "A" maintained almost the same intensity and moved southeastward. While the convective system "D" continued to develop and rapidly moved to the southwest, with the maximum intensity of corresponding radar echoes reaching 48 dBZ. The two targets of system "D" developed relatively synchronously. In addition, target "G" began to form, which can be indicated from the radar reflectivity maps. At 04:00 UTC [see Fig. 8(c)], targets "G" and "D" continued to expand, while "H" and "B" were newly formed and entered a stage of rapid growth, and the corresponding radar echoes were still below 20 dBZ for

targets "E", "F," and "I." At this moment, the CWNNet failed to predict targets "B" and "F."

At 04:15 UTC [see Fig. 8(d)], system "A" continued to move southeastward and the overall intensity tended to weaken, while a convective cell rapidly generated at the southwest boundary of "A." Meanwhile, convective systems "G" and "D" reached their mature stages, and two cells of "D" merged. At this time, targets "B", "F", "H," and "I" entered the mature stage with a rapidly accelerating rate, while "E" was less active. At this time, the CWNNet failed to predict targets "B", "C", "E", "F," and "I."
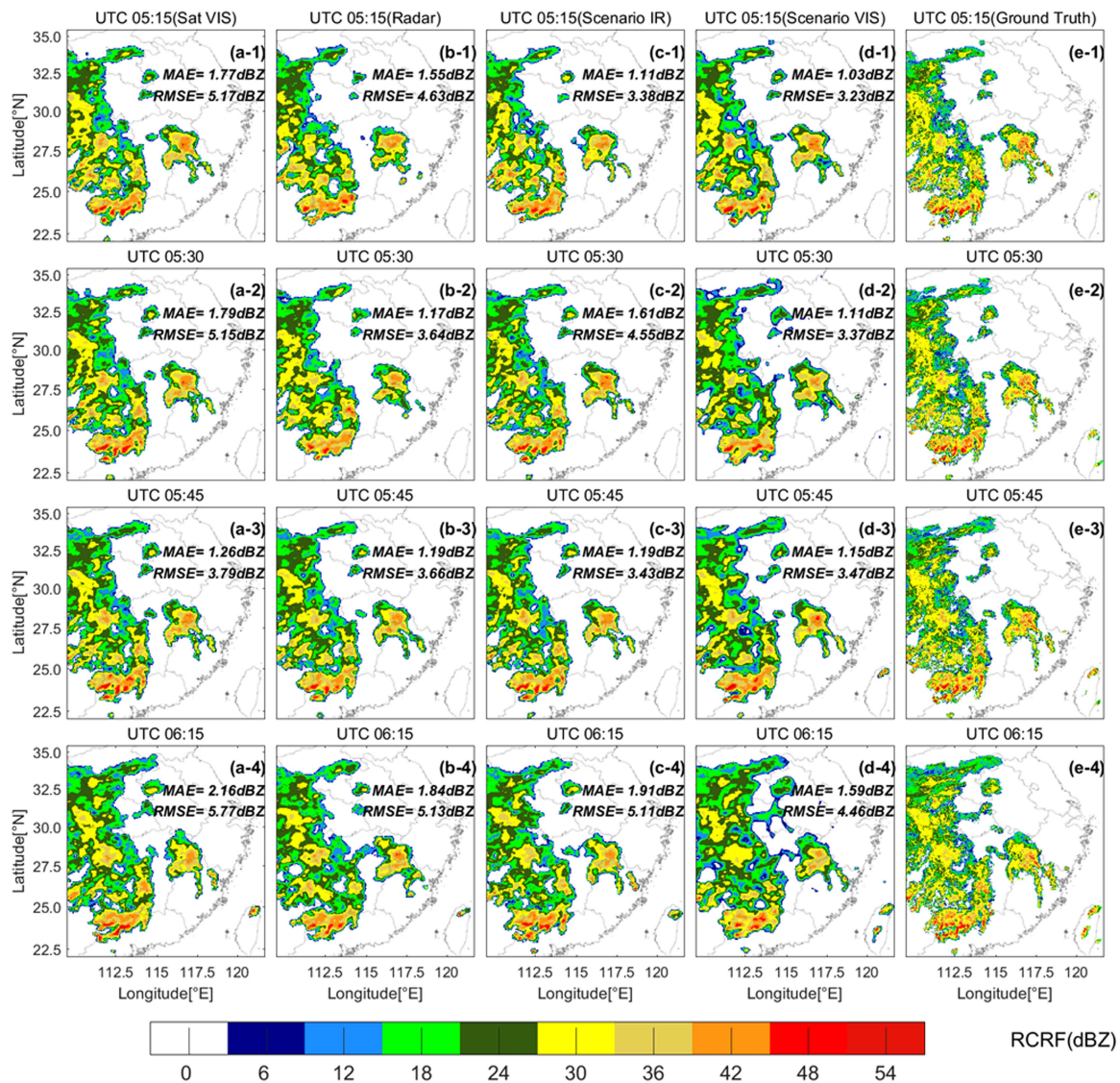
Fig. 11. Results of predicted RCRF maps of CWNNet's 1-h nowcasting from 05:15 UTC to 06:15 UTC on June 28, 2020 by using the interest fields from different sources (a) satellite visible channels, (b) radar, (c) scenario IR, and (d) scenario VIS, and (e) corresponding observed RCRF maps from ground-based weather Doppler radars.

The CWNNet is a rolling nowcasting system with the time interval of 15 min. Fig. 9 gives the prediction results for the next 30 min. In Fig. 8, the target "C" formed at 04:15 UTC was not accurately predicted by the CWNNet at 03:15 UTC (only a few pixels were successfully predicted), while Fig. 9 clearly reveals that the target "C" was successfully predicted at 03:45 UTC. Although the leading time of prediction for target "C" did not exceed one hour, it was more than 30 min, and several other initiative convections around the group of "H", "I," and "J" were also successfully predicted.

In order to evaluate the impacts of input data from different sources, this article also performs comparative experiments of 1-h nowcasting by using the interest fields from satellite visible channels, radar data, scenario IR and scenario VIS, respectively.

As displayed in Fig. 10, a group of newly emerging convective cloud clusters occurred in Southeast China during 06:45–08:15 UTC on June 28, 2019. According to the statistical metrics of

1-h convection nowcasting by the CWNNet, the TS reaches 0.82 and 0.79 for the interest fields from scenario IR and scenario VIS, respectively. The CWNNet of scenario VIS reaches the best scores among the four scenarios. In this case, the radar is not sensitive to the convection at the early stage. It misses most of the convection initiation nowcasting and the TS was 0.7475 when only the radar data is adopted as the interest fields. The CWNNet performs worse when only the satellite data is used to generate the interest fields, with the TS being 0.69.

Fig. 11 shows the predicted RCRF maps of the mesoscale convective systems happened in South China during 05:15–06:15 UTC on June 28, 2020. According to the verification scores of 0–1-h convection nowcasting by the CWNNet, the mean RMSE reaches 4.12 and 3.633 dBZ for scenario IR and scenario VIS, respectively. In this case of Taiwan Region, the radar is also insensitive to the convection at the early stage. Its prediction results on convection initiation nowcasting are relatively lagging
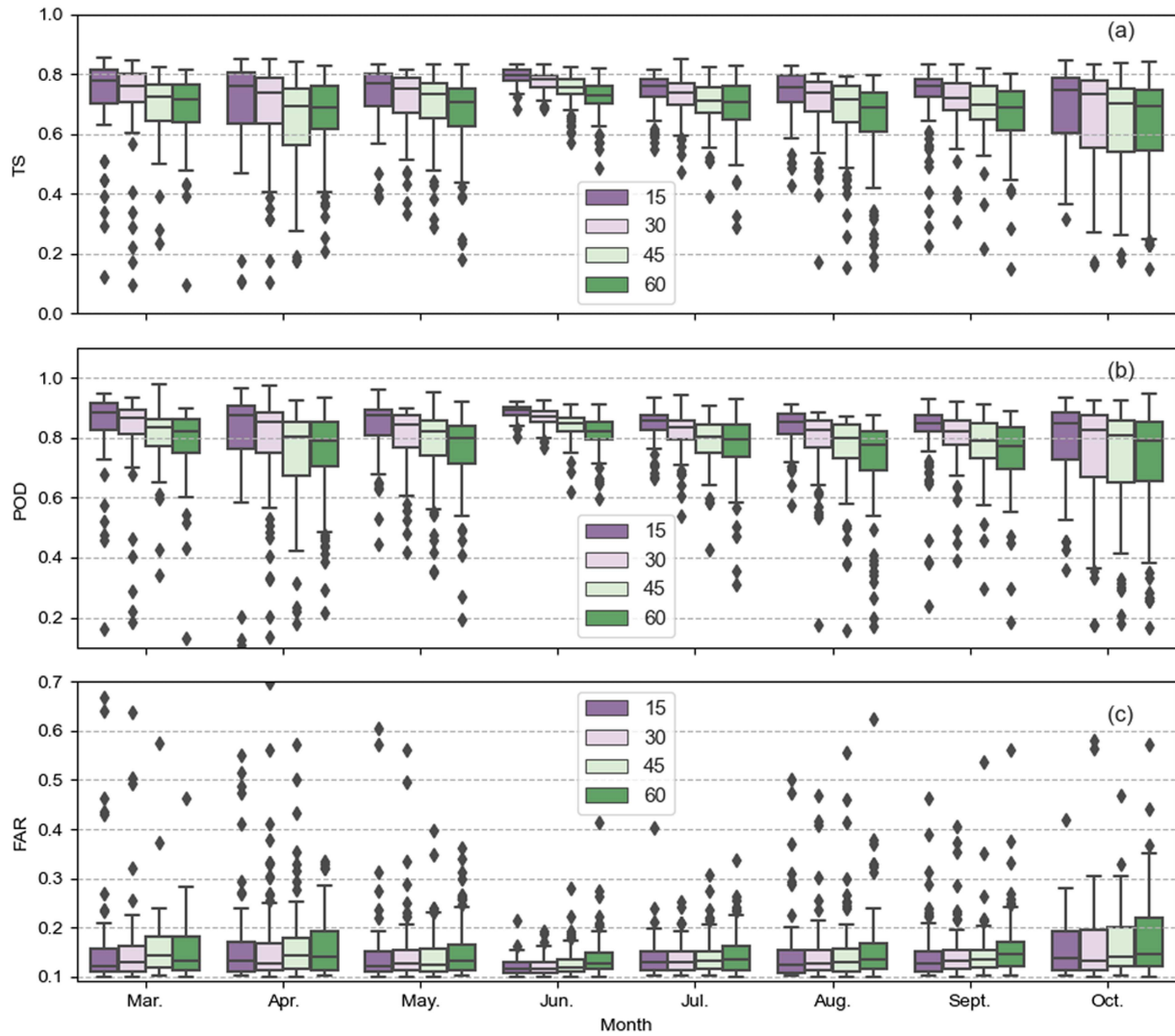
Fig. 12. Box plots of the verification scores for the 15-, 30-, 45-, and 60-min nowcasting from March to October in 2020 by the CWNNet of scenario VIS. (a) Threat score, (b) probability of detection, and (c) false alarm ratio. Boxes show the 25th, 50th, and 75th percentiles. The whiskers extend to the most extreme data points between the 75th and 25th percentiles. Outliers are marked as diamonds.

and the mean RMSE is 4.26 dBZ when only the radar data are adopted. The CWNNet performs worse when only the satellite data are used to generate the interest fields with the mean RMSE of 4.97 dBZ. Similar to Fig. 10, the phenomenon of missing also occurs in the early stage of convection. This reveals that the leading time for CI nowcasting exceeds 30 min and does not exceed 60 min.

B. Statistical Results

This section presents the statistical results of the 0–1-h nowcasting by the CWNNet. As mentioned in Section III-B, the remained one-sixth of labeled datasets in each month were utilized for model validation. Fig. 12 displays the statistical performance metrics for the CWNNet described above from March to October of 2020 using the interest fields of radar combined with visible channels. With the increase of leading time, the accuracy decreases while the uncertainty increases. It can be seen that the 1-h nowcasting of scenario VIS exhibits a good performance,

with the mean TS of 0.688–0.729, mean POD of 0.768–0.821 and mean FAR of 0.128–0.146. The statistics for June look quite a bit different. Using the OF extrapolation method, it can also be found that the standard deviation of verification scores for the OF convective extrapolation in June is low, which may be related to the relatively weak nonlinearity of convective development and the reduction of prediction difficulty in June 2020.

In order to evaluate the impacts of the inputs from different sources, this article also conducts comparison experiments on the sensitivity of the CWNNet by using four groups of input data sources, including the single satellite visible channels data, single radar data, scenario IR and scenario VIS. The verification scores for the 1-h convective weather nowcasting using the four different groups of input data sources from March to October in 2020 are shown in Fig. 13. The result using satellite observations alone gets the worst score, with a mean TS of 0.589–0.638 and a mean FAR of 0.189–0.24, while the result of scenario VIS performs the best, with a mean TS of 0.69–0.73 and a mean FAR of 0.125–0.147. The reason for the poor effect of using satellite
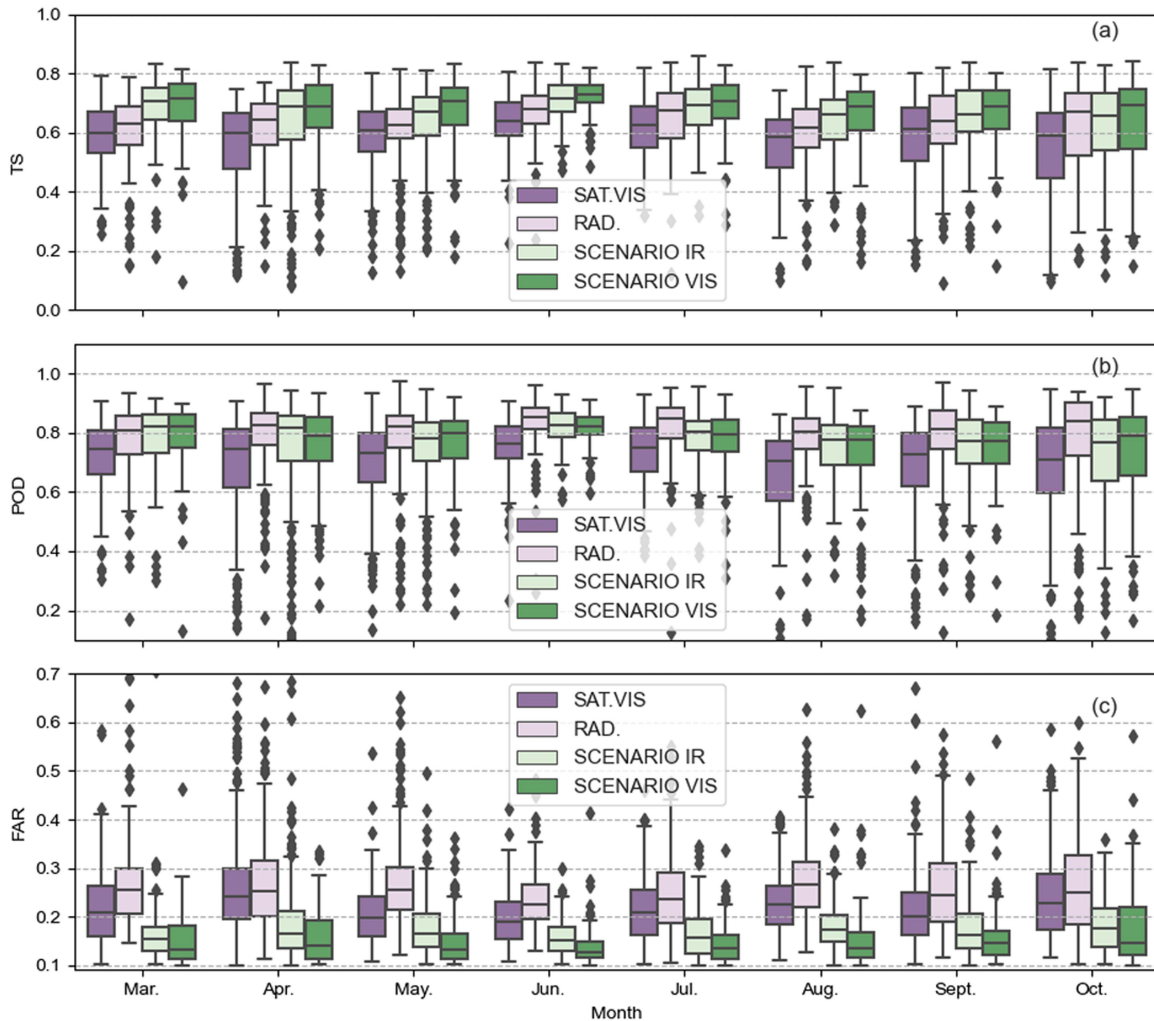
Fig. 13. Box plots of the verification scores for the 1-h convective weather nowcasting from March to October in 2020 from four different groups of input data sources including single satellite visible channels data, single radar data, scenario IR and scenario VIS. (a) Threat score, (b) probability of detection, and (c) false alarm ratio. Boxes signify the 25th, 50th, and 75th percentiles, respectively. The whiskers extend to the most extreme data points between the 75th and 25th percentiles. Outliers are marked as diamonds.

observations alone is that there is no direct relationship between the satellite and radar observations, and there is a conversion error. As the radar is less sensitive to initial convections, with which it is difficult to make predictions without indications, it always lags behind the satellite to detect the initial convections. The fusion of radar and satellite observation data can help extract the signal of convection at the early stage and thus suppress the FAR. Therefore, the result of scenario VIS performs the best.

The statistical validation results in Table V also show that using satellite observations alone performs the worst, with a mean MAE of 0.86–1.23 dBZ, and a RMSE of 2.95–4.25 dBZ, while the result of scenario VIS gets the best statistical results, with a with a mean a MAE of 0.82–1.127 dBZ, and a RMSE of 2.76–3.99 dBZ.

C. Discussions

Convectional object-oriented tracking and nowcasting algorithms using Fengyun-4A /AGRI for convective systems are based on extracting the development trends of previous existing

TABLE V
STATISTICAL VALIDATIONS ON 1-HOUR PREDICTED RCRF BY CWNNET

Application Month	Satellite VIS		Radar		Scenario IR		Scenario VIS	
	MAE	RMSE	MAE	RMSE	MAE	RMSE	MAE	RMSE
Mar.	1.10	3.40	1.11	3.30	1.04	3.07	**1.01**	**3.04**
Apr.	0.86	2.95	0.83	2.82	0.81	2.80	**0.82**	**2.76**
May.	1.23	3.90	1.25	3.85	1.20	3.79	**1.14**	**3.69**
Jun.	1.14	3.80	1.11	3.65	1.10	3.81	**1.025**	**3.50**
Jul.	1.099	3.69	1.082	3.67	1.104	3.52	**1.053**	**3.57**
Aug.	1.218	4.25	1.184	4.15	1.138	3.80	**1.127**	**3.99**
Sept.	1.099	3.42	1.082	3.45	1.104	3.41	**1.087**	**3.37**
Oct.	1.144	3.37	1.053	3.07	1.082	3.09	**1.042**	**3.00**

convective systems. In comparison with convectional nowcasting algorithms, the CWNNet with powerful feature extraction capability is able to effectively extract the features of CI and thus perform well in prediction of CI. The results from Figs. 8 and 9 reveal that the leading time for CI nowcasting exceeds 30 min. Furthermore, a comparative analysis indicates that the

radar is less sensitive to initial convections, with which it is very difficult to make predictions without indications. The fusion of radar and satellite data can help extract the signal of convections at the early stage and thus suppress the FAR.

Fig. 12 reveals that with the increase of leading time, the accuracy decreases while the uncertainty increases. The results of comparative analysis in Fig. 13 and Table V show that the 1-h nowcasting by the interest fields of satellite visible/near infrared channels combined with radar exhibits a better performance than that of infrared channels. This is because the visible/near channel is more sensitive to cloud microphysical properties than the infrared channels. From the perspective of operational application, it shows the importance of visible /near infrared channels and algorithm of CWNNet needs to be further improved when $SZA > 60°$.

In addition, the CI score varies between the local rapidly developing cumulus cloud and large-scale mesoscale convective system. It is found that the CWNNet exhibits a better performance for large-scale mesoscale convective system with the POD of 0.74–0.81 and the FAR of 0.26–0.32. In contrast, the results for local rapidly developing cumulus cloud are 0.57–0.71 for POD and 0.46–0.57 for higher FAR, respectively. This shows that the forecast uncertainty of local rapidly developing cumulus cloud is obviously greater than that of mesoscale convective system.

V. Summary

This article proposed a unified 0–1-h nowcasting algorithm for severe weather systems by using the joint observations of radar and satellite from the AGRI onboard the first of China's second generation GEO meteorological satellites of Fengyun-4A. A DL-based ConvRNN model for convective weather prediction named the CWNNet is constructed to implement the nowcasting. This new algorithm of CWNNet is different from the object-oriented tracking method (i.e., the OF method) and traditional machine learning techniques. Note that, its key advantage is the powerful ability to capture the spatial-temporal evolution information of severe convective weather. The result using the satellite observations alone gets the worst score, with a mean TS of 0.589–0.638, a mean FAR of 0.189–0.24, a mean MAE of 0.86-1.218 dBZ and a mean RMSE of 2.95-4.25 dBZ, while the result using observations from scenario VIS performs the best, with a mean TS of 0.69–0.73, a mean FAR of 0.125–0.147, a mean MAE of 0.82-1.14 dBZ and a mean RMSE of 2.76-3.99 dBZ.

Moreover, several cases of rapidly developing convections are also analyzed. The results reveal that the leading time for CI nowcasting exceeds 30 min. Furthermore, a comparative analysis indicates that the radar is less sensitive to initial convections, with which it is difficult to make predictions without indications. The fusion of radar and satellite data can help extract the signal of convections at the early stage and thus suppress the FAR. Therefore, the result using the observations from radar combined with satellite visible channels performs the best.

The fusion application of the other multi-source data will also improve the accuracy of nowcasting CI. The atmospheric temperature and humidity profiles are indispensable basic data for nowcasting of convective weather. As a result, the merits of atmospheric sounding measurements from infrared and microwave hyperspectral instrument are undoubtedly beneficial to nowcasting CI in the future.
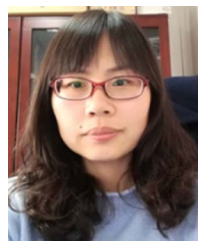
References

[1] A. Bellon and I. Zawadzki, "A 9-year summary of radar characteristics of mesocyclonic storms and of deep convection in Southern Quebec," *Atmos.-Ocean*, vol. 41, no. 2, pp. 99–120, Jun. 2003.

[2] B. T. Smith, R. L. Thompson, J. S. Grams, C. Broyles, and H. E. Brooks, "Convective modes for significant severe thunderstorms in the contiguous United States. Part I: Storm classification and climatology," *Weather Forecasting*, vol. 27, no. 5, pp. 1114–1135, Oct. 2012.

[3] P. S. Ray, Ed., *Mesoscale Meteorology and Forecasting*. Berlin, Germany: Springer, 2015.

[4] W. Schmid, S. Mecklenburg, and J. Joss, "Short-term risk forecasts of severe weather," *Phys. Chem. Earth Part B, Hydrol. Oceans Atmos.*, vol. 25, no. 10–12, pp. 1335–1338, 2000.

[5] L. L. Zheng, J. H. Sun, X. L. Zhang, and C. H. Liu, "Organizational modes of mesoscale convective systems over central East China," *Weather Forecasting*, vol. 28, no. 5, pp. 1081–1098, Oct. 2013.

[6] R. M. Cintineo and D. J. Stensrud, "On the predictability of supercell thunderstorm evolution," *J. Atmos. Sci.*, vol. 70, no. 7, pp. 1993–2011, Jul. 2013.

[7] A. L. Houston, N. A. Lock, J. Lahowetz, B. L. Barjenbruch, G. Limpert, and C. Oppermann, "Thunderstorm observation by radar (ThOR): An algorithm to develop a climatology of thunderstorms," *J. Atmos. Ocean. Technol.*, vol. 32, no. 5, pp. 961–981, May 2015.

[8] K. Wapler, F. Harnisch, T. Pardowitz, and F. Senf, "Characterisation and predictability of a strong and a weak forcing severe convective event - a multi-data approach," *Meteorologische Zeitschrift*, vol. 24, no. 4, pp. 393–410, 2015.

[9] M. Gijben and E. de Coning, "Using satellite and lightning data to track rapidly developing thunderstorms in data sparse regions," *Atmosphere*, vol. 8, no. 4, p. 67, Apr. 2017.

[10] D. S. Henderson, J. A. Otkin, and J. R. Mecikalski, "Evaluating convective initiation in high-resolution numerical weather prediction models using GOES-16 infrared brightness temperatures," *Monthly Weather Rev.*, vol. 149, no. 4, pp. 1153–1172, Apr. 2021.

[11] D. E. Buechler and S. J. Goodman, "Echo size and asymmetry: Impact on NEXRAD storm identification," *J. Appl. Meteorol. Climatol.*, vol. 29, no. 9, pp. 962–969, 1990.

[12] A. del Moral, T. Rigo, and M. C. Llasat, "A radar-based centroid tracking algorithm for severe weather surveillance: Identifying split/merge processes in convective systems," *Atmos. Res.*, vol. 213, pp. 110–120, Nov. 2018.

[13] B. L. Medina, L. D. Carey, C. G. Amiot, R. M. Mecikalski, and R. J. Blakeslee, "A random forest method to forecast downbursts based on dual-polarization radar signatures," *Remote Sens.*, vol. 11, no. 7, p. 826, 2019.

[14] F. Elizaga, S. Conejo, and F. Martin, "Automatic identification of mesocyclones and significant wind structures in Doppler radar images," *Atmos. Res.*, vol. 83, no. 2–4, pp. 405–414, Feb. 2007.

[15] M. Weber et al., "Towards the next generation operational meteorological radar," *Bull. Amer. Meteorol. Soc.*, vol. 102, no. 7, pp. E1357–E1383, Jul. 2021.

[16] Z. Feng et al., "A global high-resolution mesoscale convective system database using satellite-derived cloud tops, surface precipitation, and tracking," *J. Geophys. Res., Atmos.*, vol. 126, no. 8, 2021, Art. no. e2020JD034202.

[17] C. Goyens, D. Lauwaet, M. Schröder, M. Demuzere, and N. P. M. Van Lipzig, "Tracking mesoscale convective systems in the Sahel: Relation between cloud parameters and precipitation," *Int. J. Climatol.*, vol. 32, no. 12, pp. 1921–1934, 2012.

[18] T. Chen et al., "Potential impact of aerosols on convective clouds revealed by Himawari-8 observations over different terrain types in Eastern China," *Atmos. Chem. Phys.*, vol. 21, no. 8, pp. 6199–6220, 2021.

[19] X. Zhang, T. Wang, G. Chen, X. Tan, and K. Zhu, "Convective clouds extraction from Himawari–8 satellite images based on double-stream fully convolutional networks," *IEEE Geosci. Remote Sens. Lett.*, vol. 17, no. 4, pp. 553–557, Apr. 2020.

[20] D. Chen, J. Guo, D. Yao, Z. Feng, and Y. Lin, "Elucidating the life cycle of warm-season mesoscale convective systems in Eastern China from the Himawari-8 geostationary satellite," *Remote Sens.*, vol. 12, no. 14, 2020, Art. no. 2307.

[21] R. Lagerquist, J. Q. Stewart, I. Ebert-Uphoff, and C. Kumler, "Using deep learning to nowcast the spatial coverage of convection from Himawari-8 satellite data," *Monthly Weather Rev.*, vol. 149, no. 12, pp. 3897–3921, 2021.

[22] B. P. Shukla and P. K. Pal, "A source apportionment approach to study the evolution of convective cells: An application to the nowcasting of convective weather systems," *IEEE J. Sel. Topics Appl. Earth Observ. Remote Sens.*, vol. 5, no. 1, pp. 242–247, Feb. 2012.

[23] T. J. Schmit, M. M. Gunshor, W. P. Menzel, J. J. Gurka, J. Li, and A. S. Bachmeier, "Introducing the next-generation advanced baseline imager on GOES-R," *Bull. Amer. Meteorol. Soc.*, vol. 86, no. 8, pp. 1079–1096, Aug. 2005.

[24] K. Bessho, K. Date, M. Hayashi, A. Ikeda, and R. Yoshida, "An introduction to Himawari-8/9—Japan's new-generation geostationary meteorological satellites," *J. Meteorol. Soc. Jpn. Ser. II*, vol. 94, no. 2, pp. 151–183, 2016.

[25] J. Yang, Z. Q. Zhang, C. Y. Wei, F. Lu, and Q. Guo, "Introducing the new generation of Chinese geostationary weather satellites, Fengyun-4," *Bull. Amer. Meteorol. Soc.*, vol. 98, no. 8, pp. 1637–1658, Aug. 2017.

[26] J. R. Mecikalski and K. M. Bedka, "Forecasting convective initiation by monitoring the evolution of moving cumulus in daytime GOES imagery," *Monthly Weather Rev.*, vol. 134, no. 1, pp. 49–78, Jan. 2006.

[27] H. S. Letu et al., "Ice cloud properties from Himawari-8/AHI next-generation geostationary satellite: Capability of the AHI to monitor the DC cloud generation process," *IEEE Trans. Geosci. Remote Sens.*, vol. 57, no. 6, pp. 3229–3239, Jun. 2019.

[28] L. J. Zhao, C. F. Zhao, Y. Wang, Y. Wang, and Y. K. Ya, "Evaluation of cloud microphysical properties derived from MODIS and Himawari-8 using in situ aircraft measurements over the Southern Ocean," *Earth Space Sci.*, vol. 7, no. 5, May 2020, Art. no. e2020EA001137.

[29] J. R. Walker, W. M. MacKenzie, J. R. Mecikalski, and C. P. Jewett, "An enhanced geostationary satellite-based convective initiation algorithm for 0-2-h nowcasting with object tracking," *J. Appl. Meteorol. Climatol.*, vol. 51, no. 11, pp. 1931–1949, Nov. 2012.

[30] D. Han, J. Lee, J. Im, S. Sim, S. Lee, and H. Han, "A novel framework of detecting convective initiation combining automated sampling, machine learning, and repeated model tuning from geostationary satellite data," *Remote Sens.*, vol. 11, no. 12, Jun. 2019, Art. no. 1454.

[31] F. Sun, D. Qin, M. Min, B. Li, and F. Wang, "Convective initiation nowcasting over China from Fengyun-4A measurements based on TV-L-1 optical flow and BP_Adaboost neural network algorithms," *IEEE J. Sel. Topics Appl. Earth Observ. Remote Sens.*, vol. 12, no. 11, pp. 4284–4296, Nov. 2019.

[32] T. Rigo, N. Pineda, and J. Bech, "Analysis of warm season thunderstorms using an object-oriented tracking method based on radar and total lightning data," *Natural Hazards Earth Syst. Sci.*, vol. 10, no. 9, pp. 1881–1893, 2010.

[33] C. Munoz, L. P. Wang, and P. Willems, "Enhanced object-based tracking algorithm for convective rain storms and cells," *Atmos. Res.*, vol. 201, pp. 144–158, Mar. 2018.

[34] L. P. Wang et al., "Enhancement of radar rainfall estimates for urban hydrology through optical flow temporal interpolation and Bayesian gauge-based adjustment," *J. Hydrol.*, vol. 531, pp. 408–426, Dec. 2015.

[35] J. M. Apke, K. A. Hilburn, S. D. Miller, and D. A. Peterson, "Towards objective identification and tracking of convective outflow boundaries in next-generation geostationary satellite imagery," *Atmos. Meas. Techn.*, vol. 13, no. 3, pp. 1593–1608, Apr. 2020.

[36] L. Wang, H. Wang, and Z. W. Heng, "A rapid identification and warning method for severe weather via Doppler radar based on an improved TITAN algorithm," *J. Atmos. Sol.-Terr. Phys.*, vol. 193, Oct. 2019, Art. no. 105080.

[37] J. T. Johnson et al., "The storm cell identification and tracking algorithm: An enhanced WSR-88D algorith," *Weather Forecasting*, vol. 13, no. 2, pp. 263–276, 1998.

[38] B. P. Shukla, C. M. Kishtawal, and P. K. Pal, "Prediction of satellite image sequence for weather nowcasting using cluster-based spatiotemporal regression," *IEEE Trans. Geosci. Remote Sens.*, vol. 52, no. 7, pp. 4155–4160, Jul. 2014.

[39] D. A. Vila, L. A. T. Machado, H. Laurent, and I. Velasco, "Forecast and tracking the evolution of cloud clusters (ForTraCC) using satellite infrared imagery: Methodology and validation," *Weather Forecasting*, vol. 23, no. 2, pp. 233–245, Apr. 2008.

[40] J. R. Mecikalski et al., "Probabilistic 0-1-h convective initiation nowcasts that combine geostationary satellite observations and numerical weather prediction model data," *J. Appl. Meteorol. Climatol.*, vol. 54, no. 5, pp. 1039–1059, 2015.

[41] D. Ahijevych, J. O. Pinto, J. K. Williams, and M. Steiner, "Probabilistic forecasts of mesoscale convective system initiation using the random forest data mining technique," *Weather Forecasting*, vol. 31, no. 2, pp. 581–599, Apr. 2016.

[42] L. Han, J. Z. Sun, W. Zhang, Y. Y. Xiu, H. L. Feng, and Y. J. Lin, "A machine learning nowcasting method based on real-time reanalysis data," *J. Geophys. Res.-Atmos.*, vol. 122, no. 7, pp. 4038–4051, Apr. 2017.

[43] C. Y. Luo, X. T. Li, Y. L. Wen, Y. M. Ye, and X. F. Zhang, "A novel LSTM model with interaction dual attention for radar echo extrapolation," *Remote Sens.*, vol. 13, no. 2, p. 164, Jan. 2021.

[44] W. Fang, L. Pang, W. N. Yi, and V. S. Sheng, "AttEF: Convolutional LSTM encoder-forecaster with attention module for precipitation nowcasting," *Intell. Automat. Soft Comput.*, vol. 30, no. 2, pp. 453–466, 2021.

[45] P. Han, W. Wang, Q. Shi, and J. Yang, "Real-time short-term trajectory prediction based on GRU neural network," in *Proc. IEEE/Amer. Inst. Aeronaut. Astronaut. 38th Digit. Avionics Syst. Conf.*, 2019, pp. 1–8.

[46] L. Tian, X. Li, X. Ye, P. Xie, and Y. Li, "A generative adversarial gated recurrent unit model for precipitation nowcasting," *IEEE Geosci. Remote Sens. Lett.*, vol. 17, no. 4, pp. 601–605, Apr. 2020.

[47] X. Shi, Z. Chen, H. Wang, D.-Y. Yeung, W. Wong, and W. Woo, *Convolutional LSTM Network: A Machine Learning Approach for Precipitation Nowcasting*. Cambridge, MA, USA: MIT Press, 2015.

[48] Y. Wang, M. Long, J. Wang, Z. Gao, and P. S. Yu, "PredRNN: Recurrent neural networks for predictive learning using spatiotemporal LSTMs," 2017.

[49] X. J. Shi et al., "Deep learning for precipitation nowcasting: A Benchmark and a New Model," *Adv. Neural Inf. Process. Syst.*, vol. 30, pp. 5622–5632, 2017.

[50] Y. A. Geng et al., "Lightnet: A dual spatiotemporal encoder network model for lightning prediction," in *Proc. 25th Assoc. Comput. Machinery SIGKDD Int. Conf. Knowl. Discov. Data Mining*, 2019, pp. 2439–2447.

[51] W. Zhang, L. Han, J. Sun, H. Guo, and J. Dai, "Application of multi-channel 3D-cube successive convolution network for convective storm nowcasting," in *Proc. IEEE Int. Conf. Big Data*, 2019, pp. 1705–1710.

[52] K. H. Zhou, Y. G. Zheng, W. S. Dong, and T. B. Wang, "A deep learning network for cloud-to-ground lightning nowcasting with multi-source data," *J. Atmos. Ocean. Technol.*, vol. 37, no. 5, pp. 927–942, May 2020.

[53] X. Wang, M. Min, F. Wang, J. Guo, B. Li, and S. Tang, "Intercomparisons of cloud mask products among Fengyun-4A, Himawari-8, and MODIS," *IEEE Trans. Geosci. Remote Sens.*, vol. 57, no. 11, pp. 8827–8839, Nov. 2019.

[54] M. Steiner, J. A. Smith, and R. Uijlenhoet, "A microphysical interpretation of radar reflectivity-rain rate relationships," *J. Atmos. Sci.*, vol. 61, no. 10, pp. 1114–1131, May 2004.

[55] S. Y. Matrosov, A. J. Heymsfield, and Z. Wang, "Dual-frequency radar ratio of nonspherical atmospheric hydrometeors," *Geophys. Res. Lett.*, vol. 32, no. 13, Jul. 2005, Art. no. L13816.

[56] F. Sun, B. Li, M. Min, and D. Qin, "Deep learning-based radar composite reflectivity factor estimations from Fengyun-4A geostationary satellite observations," *Remote Sens.*, vol. 13, no. 11, 2021, Art. no. 2229.

[57] N. Xu, B. Price, S. Cohen, J. M. Yang, and T. Huang, "Deep interactive object selection," in *Proc. IEEE Conf. Comput. Vis. Pattern Recognit.*, 2016, pp. 373–381.

[58] S. Postalcioglu, "Performance analysis of different optimizers for deep learning-based image recognition," *Int. J. Pattern Recognit. Artif. Intell.*, vol. 34, no. 2, Feb. 2020, Art. no. 2051003.

Fenglin Sun received the B.S. degree in telecommunication from Ocean University of China, Qingdao, China, in 2009 and the Ph.D. degree in the electromagnetic and microwave technology from the University of the Chinese Academy of Sciences, Beijing, China, in 2014.

He is currently an Associate Professor with the National Satellite and Meteorological Center, China Meteorological Administration, Beijing, China. His research interests include convective initiation algorithms of satellite, and calibration of FengYun satellite active and passive microwave sensors.

Min Min received the B.S. degree in applied meteorology from the Nanjing University of Information Science and Technology, Nanjing, China, in 2005 and the Ph.D. degree in the atmospheric physics and environment from the Institute of Atmospheric Physics, Chinese Academy of Sciences, Beijing, China, in 2010.

He is currently an Associate Professor with the School of Atmospheric Sciences, Sun Yat-sen University, Guangdong, China. From 2010 to 2019, he was with National Satellite and Meteorological Center, China Meteorological Administration, Beijing, China. From 2013 to 2014, he was a Research Assistant with the Department of Physics, University of Maryland at Baltimore County. His research interests include cloud and weather algorithms of satellite, atmospheric radiative transfer, and calibration of FengYun satellite sensor.

Bo Li received the B.S. degree in atmospheric science from the Nanjing University, Nanjing, China, in 2006 and the Ph.D. degree in meteorology from the Institute of Atmospheric Physics, Chinese Academy of Sciences, Beijing, China, in 2011.

She is currently an Associate Professor with the National Satellite and Meteorological Center, China Meteorological Administration, Beijing, China. Her research interests include cloud phase algorithms of FengYun satellite and atmospheric circulation.

Danyu Qin received the Ph.D. degree in satellite meteorology from the Nanjing University of Information Science and Technology, Nanjing, China, in 2004.

He is a Senior Scientist and the Deputy Director of the Institute of Satellite Meteorology of the National Satellite Meteorological Center, China Meteorological Administration, Beijing, China. His studies focus on mesoscale convection activities, especially from the view of satellite. He has experience in Fengyun satellite ground segment construction. He is in charge of FY-4 (02 batch) application validation system) and FY-3 (03 batches) product generation system. He had developed the convection initiation algorithm for Fengyun-4A satellite. He is interesting in satellite weather, and engaged in remote sensing applications of Fengyun satellites.

Dr. Qin was the recipient of the first prize of Scientific and Technological Development of China Meteorological Administration in 2005.